Results in Engineering 22 (2024) 102244

Contents lists available at ScienceDirect

Results in Engineering

journal homepage: www.sciencedirect.com/journal/results-in-engineering

Review article

Recent developments in graphitic carbon nitride (g-C_3N_4) applications in micromotors

Manoj P. Rayaroth [a], Giehyeon Lee [b], Yoon-Seok Chang [c,*]

[a] Department of Life Sciences, School of Science, GITAM (Deemed to Be) University, Visakhapatnam, 530045, India
[b] Dept. of Earth System Sciences, Yonsei University, Yonsei-ro 50, Seodaemun-gu, Seoul, 03722, Republic of Korea
[c] Department of Civil, Urban, Earth and Environmental Engineering, Ulsan National Institute of Science and Technology, Ulsan, 44919 Republic of Korea

ARTICLE INFO

Keywords:
Graphitic carbon nitride
Micronanomotors
Propulsion
Environmental remediation
Water purification
Organic pollutants

ABSTRACT

Polymeric graphitic carbon nitride (g-C_3N_4) is an emerging metal-free and visible-light-active photocatalyst with much interest in various fields such as environmental and biomedical fields. The creation of photocatalysts as micro nanomotors, which can perform reactions in micro nanoscales in complex environments has widened their utility in those fields. g-C_3N_4 can act as a photocatalyst and adsorbent, hence they are widely used in environmental remediation. This applicability opens up their extension in micro and nanomotor fields. This review focuses on the fundamentals and applications of g-C_3N_4 micromotors, especially in environmental remediation. Depending on the morphology of the supporting materials, the g-C_3N_4 micromotor undergoes self-electrophoresis, self-diffusiophoresis, or bubble propulsion to move through the matrix under visible light irradiation. The motion of the particle simultaneously results in the generation of various reactive oxygen species and is utilized in the degradation of organic pollutants. The main advantage of g-C_3N_4 micromotors is that it does not require any toxic metal support and hence, can be applied in environmental remediation with minimal secondary pollution. However, most of the studies discussed in this review were carried out on a laboratory scale with limited solution volume. Therefore, a more comprehensive analysis is necessary for the implementation of the material in large-scale applications.

1. Introduction

Nanotechnology has attracted attention in various multidisciplinary applications, such as environmental (pollutant sensing, and remediation), energy production and storage, and optical and electrochemical applications. However, one of the limiting factors in any nanomaterial-assisted application is the restricted nature of their diffusion through a complex matrix [1–4]. Micronanomotors (MNMs) are emerging devices in nanotechnology that can facilitate reactions in complex fluid matrices via micromixing and mass transfer effects; they are nano- or micro-sized stimuli-responsive devices that can move through a complex matrix [5–9]. MNMs respond to stimuli such as light, magnetic fields, ultrasound, and certain chemicals in an asymmetric system [10–13]. However, MNMs that utilize chemical fuels require high concentrations of chemicals that are not eco-friendly and may cause cell damage [12,14]. There are thermal and sound methods for the propulsion of MNMs, but they are energetically unfavorable. Therefore, light-driven (especially visible light or near-infrared (NIR)) processes are beneficial in the environmental application of MNMs [10,15–17]. Another important factor determining the micromovement of the particle is its asymmetry. Janus microsphere, chiral structure, and 3D-particle with unconventional shapes are some of the asymmetric structures. The effectiveness in the applications of the micromotors strongly depends on their materials and morphology [18,19].

Recently, photocatalytic materials have been widely used in conjunction with light-driven MNMs; these materials are easily synthesized and convert light and chemical energy into mechanical energy [17,20]. The mechanism involved in light-driven MNMs is the electron transfer reaction between the valence band and the conduction band of the material. The resulting electron-hole ($e^{-}-h^{+}$) pair participates in the reaction with the water molecule or other chemical species present in the liquid medium. This is followed by self-electrophoresis, diffusiophoresis, and bubble ejection concerning the asymmetry generated in the structure or nature of the chemical species present in the liquid

---

* Corresponding author. Department of Urban and Environmental Engineering, Ulsan National Institute of Science and Technology, Ulsan, 44919 Republic of Korea.

E-mail address: chang.yoonseok@postech.ac.kr (Y.-S. Chang).

https://doi.org/10.1016/j.rineng.2024.102244
Received 11 February 2024; Received in revised form 28 April 2024; Accepted 8 May 2024

medium (Fig. 1) [20,21]. In the Janus spherical micromotor, the asymmetric allocation of ions around the micromotor results in a self-generated electric field (self-electrophoresis). The diffusion of ionic or non-ionic products formed by the photocatalytic reaction at one face of the materials results in the generation of an electric field (self-diffusiophoresis), which can propel the micromotor by inducing an electrokinetic flow via the surface charge coupling of the particles. In the case of bubble propulsion mechanisms, the charge carriers oxidize water molecules or H_2O_2 or reduce the H^+ ions to form O_2 and H_2 bubbles, respectively, depending on the nature of the material [22]. Notably, the bubble propulsion phenomenon is stronger in fuel-added systems [23–26].

Previously, photocatalysts such as TiO_2, ZnO, and BiOI have been used for MNM applications, among which the TiO_2-based materials are the most studied [17,27–31]. Strong UV light is required for the self-diffusiophoresis of the TiO_2 plane. However, the modification of TiO_2 with Au or Pt can lower the UV light intensity and shift the propulsion mechanism to self-electrophoresis [20,29,32,33]. Chemical fuels, especially H_2O_2, enhance the movement of MNMs by generating bubbles. The plain tubular photocatalytic MNMs and Pt coated on the inner layer of the particles propel the material via a bubble ejection-propulsion mechanism. The supporting material converts H_2O_2 into O_2 bubbles (Eqn (1)) [34,35]:

$$H_2O_2 \text{ (supporting materials)} \rightarrow H_2O + ½\, O_2 \quad (1)$$

However, TiO_2-based materials are less reactive in the visible light region. Additionally, the use of materials such as Au and Pt makes the fabrication process expensive. Hence, current research focuses on the use of visible-light-active, eco-friendly, and cost-effective materials for MNMs [17,32,36–38]. Polymeric graphitic carbon nitride (g-C_3N_4), a metal-free polymeric semiconductor material, has been used in optical and electronic devices, in environmental applications, and as energy. g-C_3N_4 has several advantages over other metal oxide semiconductors, such as a facile synthesis, chemical and thermal stability, visible light activity (band gap of 2.7 eV), biocompatibility, and sustainability [39–44]. The extended absorption in visible light makes it more convenient in many kinds of photochemical reactions. In addition to carbon and nitrogen, the g-C_3N_4 has hydrogen specifically coming from the precursor materials. It has an N-bridged structure of poly(triazine) and poly(tri-s-triazine) repeat units and contains defects [45]. As a result, many chemical reactions are feasible in g–C_3N_4–based catalytic systems. Delocalized electron cloud exists in their structure owing to the sp^2 hybridization of C and N. Due to the above properties, g-C_3N_4 has been widely used for various applications such as organic synthesis, CO_2 reduction, photocatalytic water splitting for H_2 production, decontamination, oxidant activation, etc. There are many reviews already reported for the above applications of g-C_3N_4 [46–48].

1.1. Micromotors for water purification

Water pollution by organic and inorganic contaminants is of major concern as it limits access to pure water [49–52]. As a result of various activities pollution goes on increasing and many people lack safe drinking water. Therefore many techniques (both physical and chemical methods) have evolved in the removal of the contaminants [53–56]. Nanomaterials are successfully applied in the removal of almost all contaminants (often called nanoremediation) [57–60]. These materials favored the removal either through adsorption or oxidation depending on properties such as surface area, surface charge density, and chemical affinity. The heavy metals and some of the organic contaminants depending on the surface charge density of the materials and pollutants can be effectively removed by adsorption and on the other hand the generation of reactive species by the materials leads to the mineralization of organics. The oxidative process is usually done by photo-irradiation on the material surface. Several photocatalytic materials were developed for this objective for the oxidation of organic contaminants [61–65]. In short, nanoremediation is applied in environmental matrices such as soil, air, and water [56].

To extend nano remediation, researchers have developed various micromotors of those materials for environmental remediation. Based on the nature of the MNMs, the pollutants can be removed by adsorption or oxidation. The previous studies reported that activated carbon-based micromotors removed the heavy metals through adsorption. Photocatalytic micromotors were releasing the reactive oxygen species during their propulsion. MNMs of TiO_2, ZnO, and BiOI are utilized in the oxidative removal of various contaminants [17,27–31]. The g-C_3N_4 as a photocatalytic material for environmental remediation has several advantages such as visible light absorption, electron-hole recombination rate, and catalytic reaction. As a result, several studies reported the removal of pollutants using g-C_3N_4 promisingly due to the properties described in the previous section [66–69]. Recently, the applications of g-C_3N_4 in MNMs are emerged and some researchers studied their different motion behaviors followed by their environmental applications. Therefore, this review focuses on the application of g-C_3N_4 in MNMs. Various methods for the fabrication of g-C_3N_4 MNMs, properties, trajectories, and driving force for the propulsion, and finally their environmental remediation are discussed in the following sections. However, no proper reviews are available regarding this topic. Therefore this review will help advance the research on g-C_3N_4 MNMs, especially for the water treatment which will subsequently lessen the water crisis.

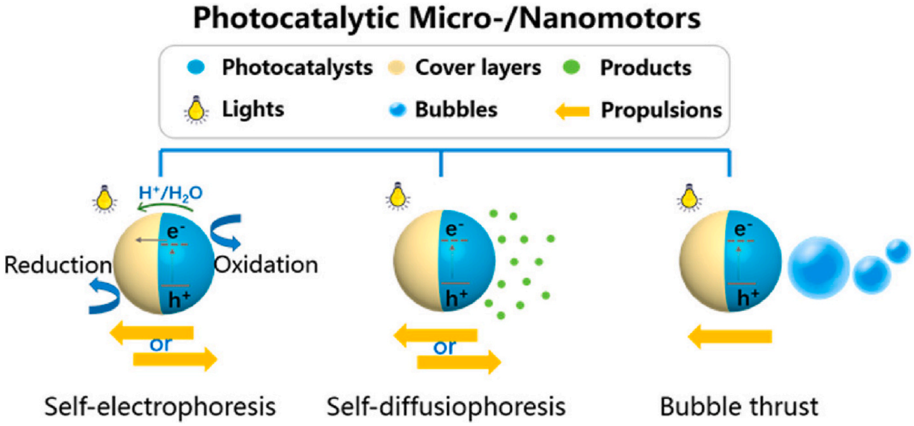

Fig. 1. Various mechanisms involved in the propulsion of photocatalytically active MNMs: "Reprinted (adapted) with permission from Ref. [16]. Copyright 2018 American Chemical Society.

1.2. Fabrication, and properties of g-C_3N_4 micromotors

g-C_3N_4 is synthesized via the temperature-assisted polymerization of nitrogen-enriched compounds with pre-bonded C–N core structures, such as urea and melamine [40,70–73]. The treatment process varies based on the desired shape of the catalysts. The simple calcination of urea or melamine at 550 °C is used to synthesize sheet-like g-C_3N_4; the solvothermal method produces spherical g-C_3N_4 [74]. Fig. 2 details the various fabrication methods of g-C_3N_4 micromotors. Modifications are also carried out on the synthesized g-C_3N_4 to obtain the required shapes and compositions of the material.

Table 1 details the various shapes of g-C_3N_4 in MNM applications. The application of g-C_3N_4 in MNMs was studied by Ye et al., such that they synthesized spherical g-C_3N_4 micromotors that were modified with various materials, such as Pt-g-C_3N_4 and Pt-g-C_3N_4/Fe_3O_4. The g-C_3N_4 sheets were synthesized via the thermal treatment of urea. Subsequently, 20 mL of aqueous g-C_3N_4 sheets were treated with 0.01 M chloroplatinic acid and then sonicated. The mixture was then reduced with $NaBH_4$ and sonicated further to yield Pt-g-C_3N_4 sheets. Then, 5 wt% of PVP solution (Fe_3O_4 is added to PVP solution for the synthesis of Pt-g-C_3N_4/Fe_3O_4) and 30 mL olive oil containing 1 mg surfactant, span 80 was added to the nanosheet solution and stirred constantly for approximately 15 min. The mixture was then heated at 90 °C for approximately 2 h. The synthesized motor had a smooth surface and was spherical with an average size of 2.6 μm [78]. The synthesized micromotors have a larger surface area compared to the normal g-C_3N_4. The stacked conjugated aromatic system of g-C_3N_4 was confirmed from the XRD peak at 27.2°. The visible light activity is coming from their light absorption at 320 nm. FTIR also given structural characteristics such as the presence of tri-s-triazine units (peak at 810 cm^{-1}, bending vibration), C–N (stretching vibrational bands at 1070, 1419, and 1570 cm^{-1}), C═N stretching (1627 cm^{-1}). A graphitic sp^2 bond was further confirmed from a peak at 1620 cm^{-1} in the Raman spectra.

Spherical g-C_3N_4 can be synthesized from sheet-like g-C_3N_4. For this, the g-C_3N_4 sheets were ground well with potassium thiocyanate (KSCN) and dried in a vacuum oven at 140 °C for approximately 12 h. The product was then heated at a temperature gradient of 400–500 °C for approximately 2 h under the Ar atmosphere to yield a spherical shape. The resulting product was then washed, centrifuged, and dried [77]. Rayaroth et al. synthesized a spherical Janus Fe-g-C_3N_4 micromotor with a diameter of 1 μm. The spherical g-C_3N_4 was synthesized via the solvothermal reaction of cyanuric chloride in acetonitrile at 200 °C. The

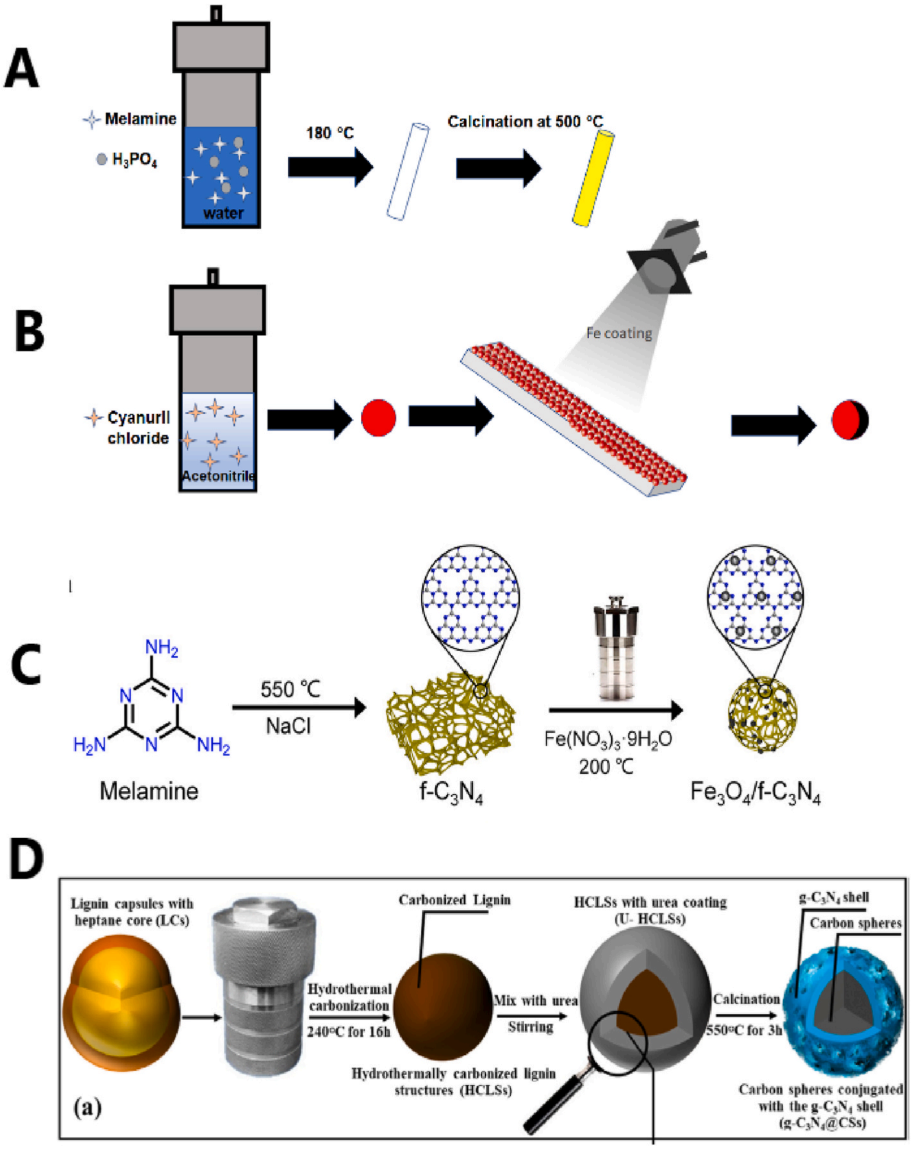

Fig. 2. Synthesis procedure for (A) tubular g-C_3N_4 micromotor, (B) spherical micromotor, (C) Fe_3O_4/f-C_3N_4 adapted from Ref. [75] Copyright 2022 American Chemical Society and (D) g-C_3N_4 @CS [76] Copyright 2022 American Chemical Society.

Table 1

Shape, velocity, and propulsion mechanism of various g-C_3N_4 micromotors.

Propulsion of micromotor				Environmental Remediation			
Micromotor (shape)	Propulsion mechanism	Experimental conditions	Velocity (V) or Diffusion (D)	Pollutant	Experimental conditions	Degradation efficiency	Ref:
Fe_3O_4/3-D porous foam-like C_3N_4 (f-C_3N_4) (Spherical)	Bubble propulsion	Visible light, intensity 300 mW cm^{-2}, 0.2 wt % H_2O_2	D = 1.77 μm^2 s^{-1}	Tetracycline	$[C]_0 = 30$ ppm, $[H_2O_2] = 2$ %, intensity 300 mW cm^{-2}	96.4 % removal in 90 min	[75]
Pt/Pd@g–C_3N_4–carbon sphere (Spherical)	Bubble propulsion	Visible light, intensity 880 mW cm^{-2}, 7.5 wt % H_2O_2	V = 14.5 ± 3.4 μm s^{-1}	Rhodamine B	$[C]_0 = 5$ ppm, [micromotor] = 1 mg/3 mL, visible-light source	99 % degradation in 180 min	[76]
Fe/C_3N_4 (Spherical)	Self-electrophoretic mechanism and liquid phase bubble generation	A green laser beam available in NTA system, Cr(VI) = 5 ppm, H_2O_2 = 0.5 vol %,	D = 44 × 10^6 nm^2 s^{-1}	Sulfamethoxazole	$[C]_0 = 1$ ppm, [Cr(VI)] = 5 ppm, $[H_2O_2] = 0.5$ %	100 % removal in 8 min	[79]
g–C_3N_4–coated on carbon microsphere (Spherical)	Bubble propulsion	Blue light, intensity 250 mW cm^{-2}, 30 wt % H_2O_2	V = 107.22 μm s^{-1}	Rhodamine B	$[C]_0 = 10$ ppm, [micromotor] = 20 mg in 50 mL $[H_2O_2] = 3$ %, [SDS] = 0.125 wt%, visible light	98.9 % degradation in 60 min	[80]
Fe_3O_4/C_3N_4 (tubular)	Bubble propulsion	visible light, intensity 250 mW cm^{-2}, 30 wt % H_2O_2	V = 178.9 μm s^{-1}	Rhodamine B	$[C]_0 = 10$ ppm, [micromotor] = 20 mg in 50 mL $[H_2O_2] = 3$ %, [SDS] = 0.125 wt%, visible light	99.8 % in 60 min	[81]
g-C_3N_4 (Tubular)	Bubble propulsion	Visible light, Intensity, 0.88 Wcm^{-2}, 20 wt% H_2O_2, 0.25 wt% SDS	V = 72 ± 6 μm s^{-1}	Heavy metal, Cu^{2+}	$[C]_0 = 1$ ppm, $[H_2O_2] = 5$ wt%	100 % removal in 7 min	[82]
3D-printed/Fe_3O_4/C_3N_4 (Hollow tube)	Bubble propulsion by H_2 bubbles	Visible light	V = 210 μm s^{-1}	Picric acid	$[C]_0 = 10 \times 10^{-3}$ M, Visible light	38 % in 10 min	[83]

dried materials in ethanol were then sonicated to obtain a good material dispersion and drop cast on the glass slide [79]. The dried glass slide containing spherical g-C_3N_4 is then coated with Fe, Au, Pd, or Pt via the sputter coating method. The elemental composition of g-C_3N_4 micromotor was obtained from XPS analysis. The high-resolution XPS spectra of C1s showed the peaks for graphitic carbon (284.8 eV), C–C/adventitious carbon (286.7 eV), and sp^2-hybridized carbon from C–N=C and N–$(C)_3$ (289.4 eV). In the same way, N1s showed the peaks correspond to that in in triazine rings (397.4 eV), tertiary nitrogen (398.9 eV), and amino group (400.3 eV). In Janus Fe-g-C_3N_4, iron nitride bond formation has occurred after the Fe coating as confirmed by XPS spectra. In the XPS spectra the peaks corresponding to Fe 2p, N 1s, are C 1s were shifted to higher binding energies after Fe doping, an indication of bond formation or Fe permeation. All other properties were matched with those of the g-C_3N_4 micromotors.

The 3D-porous foam-like g-C_3N_4 (f-g-C_3N_4) was synthesized via the thermal condensation of melamine mixed with NaCl. The hydrothermal reaction of the above product with $Fe(NO_3)_3$ resulted in the deposition of Fe_3O_4 on the C_3N_4 [75]. The presence of micro nanopores in the f-g-C_3N_4 structure resulting a different interplanar periodicity compared to bare g-C_3N_4 and hence a shifting of XRD peaks representing tris-s-triazine units (d_{100}) was reported. However, after the deposition of Fe_3O_4, the micromotor loss interplanar periodicity and Fe_3O_4 peaks become prominent in XRD. In the FTIR spectra, a peak corresponds to the Fe–O vibration (580 cm^{-1}) showing an effective bonding during their fabrication. The interaction of Fe_3O_4 with triazine results in the shift of absorption peaks at 801-811 cm^{-1}. The N–H groups (sharp FTIR peak at 3288 cm^{-1}) were more exposed on the surface of the micromotor after the hydrothermal process. The oxygen content is relatively high compared to g-C_3N_4 due to the presence of carboxyl and Fe–O groups.

The g–C_3N_4–coated carbon microsphere (CMS) was synthesized in the same way by mixing g-C_3N_4 and CMSs. A co-calcination of a mixture of carbonized lignin structures and urea resulted in the formation of g–C_3N_4–coated CMS. The metal deposition on the MNM was done by the sputter coating method [76,80]. A complete trapping of CMS into g-C_3N_4 with high uniformity occurred in this process. This micromotor has a diameter of 13 μm. The stacked spaces of 2D g-C_3N_4 resulting the formation of pores on the micromotor surface. The hydroxylation reaction between terminal amino groups (C–N–H) of g-C_3N_4 and hydroxyl and carboxy group of CMS resulting a lamellar g-C_3N_4 self-assembly on CMSs and reduced the O content in g-C_3N_4@CMS.

Tubular g-C_3N_4 micromotors were synthesized via the hydrothermal treatment of melamine with H_3PO_4. The solid samples were washed with Milli-Q water and calcined at 500 °C for 4 h. The synthesized MNMs had C and N in their tubular structure with an average diameter of 9.7 ± 1.5 μm and a length of 67 ± 14 μm, which was confirmed via SEM analysis; these MNMs also exhibited fluorescent properties and were translucent. Notably, Zheng et al. also synthesized a tubular g-C_3N_4/Fe_3O_4 via the template-assisted hydrothermal treatment method [81,82]. The XRD peaks corresponding to g-C_3N_4 and Fe_3O_4 in g-C_3N_4/Fe_3O_4 were weakened compared to their materials indicating an interaction of these materials and less crystalline. XPS spectra and the elemental analysis show their structure same as other g-C_3N_4 micromotors.

In summary, one- and two-stage methods have been utilized for the synthesis of g-C_3N_4 –based micromotors. In all methods, the first step was the thermal treatment of urea or melamine. The obtained micromotor exhibited good absorptivity in the visible light region. The translucent behavior of some of the micromotor will be able to monitor their bubble propulsion mechanism. All those properties make them a good candidate for their micromotor applications.

1.3. *Propulsion of g-C_3N_4 micromotors*

The roles of fuel-free and fueled g-C_3N_4 micromotors have been extensively studied. Optical microscopes were used to monitor the propulsion and motion behavior of the micromotors in most studies [84]. Dynamic light scattering was used in some cases [85,86]. Rayaroth et al. used a nanoparticle tracking analyzer (NTA) to study the motion of the MNM [79]. Like other photocatalytic mechanisms, the photoirradiation on the surface of g-C_3N_4 results in an e^-– h^+ pair (Eqn (2)). The oxidation of water molecules by the h^+ results in the formation of O_2, while the reduction of H^+ by the e−leads to the formation of H_2 (Eqns (3)–(5)) [87–89]. In the case of metal doping, the electrons are transported to and stored in the metal-doped layer of the micromotor and form a local electric field due to the charge gradient. In the fueled micromotor, the added fuel (Eg: H_2O_2) was decomposed by the electron-rich center in the material to form O_2 bubbles in the medium [27]. These reactions resulted in the movement of the material through the liquid matrix.

$$C_3N_4 + hv \rightarrow h^+ + e^-, \tag{2}$$

$$2H_2O + h^+ \rightarrow O_2 + 4\,H^+, \tag{3}$$

$$2H^+ + 2\,e^- \rightarrow H_2, \tag{4}$$

$$H_2O_2 + {}^{\bullet}OH \rightarrow 2H_2O + O_2. \tag{5}$$

The trajectory and speed of the MNMs in a liquid medium depend on the morphology and propulsion force. Ye et al. designed photocatalytically active spherical Pt/g-C_3N_4, which is negatively charged in water. The motion of the micromotor was entirely controlled by light, such that no chemicals or fuel were required. Notably, the synthesized micromotor exhibited phototactic behavior only at sizes in the range of 0.7–2 μm. However, the micromotor became immobile when the size exceeded 5 μm. The photoirradiation on the Pt/g-C_3N_4 MNMs results in the formation of various ionic products such as H^+ ions, ${}^{\bullet}OH$, and $O_2^{\bullet -}$, all of which exhibit different diffusion rates. An electrophoretic propulsion mechanism was proposed due to the negative surface charge of the Pt/g-C_3N_4 micromotor. The speed of the Pt/g-C_3N_4 was 14 μm s^{-1} in pure water, it was enhanced to 47 μm s^{-1} with the addition of 0. 1 M MeOH. On the other motion was completely stopped by the addition of NaCl. Chemical potential is the major factor in determining the diffusiophoretic propulsion. The chemical potential value and hence the movement decreased with the addition of NaCl [78].

The tubular g-C_3N_4 micromotor was propelled under visible light irradiation by a bubble propulsion mechanism. In this case, H_2O_2 was added as the fuel. The ${}^{\bullet}OH$ is generated by the reaction of electrons with H_2O_2, then further expels O2 through their with ${}^{\bullet}OH$. These bubbles are formed inner part of the tube. The bubble was formed inside the tube and was subsequently ejected through one side to propel the micromotor in the opposite direction [54]. It is to be noted the decomposition of H_2O_2 might happen both inside and outside of a tube for a single-component tubular photocatalytic system. On the other hand, the nucleation of the bubbles is thermodynamically more favorable inside the tube resulting in the formation of bubbles at a higher rate there compared to the outside of the microtube [90]. The bubble growth was also facilitated by an internal diameter of 10 μm, which is larger than those required for the bubble stable growth (0.6 μm). In the case of g-C_3N_4/Fe_3O_4 tubular micromotors, the decomposition of H_2O_2 by Fe^{3+} (to regenerate Fe^{2+}) acts as an additional source of O_2 bubbles for the propulsion of the micromotor. Similar to tubular g-C_3N_4 micromotors, the bubbles are formed inside the cavity and are ejected from one of the open faces. Moreover, depending on the length of the tube, the micromotor moves straight and rotates without any displacement [53]. Compared to bare tubular micromotor, they can move either in a straight direction or rotate without any displacement depending on the bubble expulsion from one end or both ends of the tube. It further depends on the length of the tube. The rotation of the micromotor happens only if the length of the tube is sufficiently long.

Sridhar et al. studied the propulsion of g-C_3N_4 micromotors with capping materials such as Au and Pt. The Pt-capped materials were found to move at a velocity of 10.4 ± 0.6 μm s^{-1}, and the Au swimmer moved at a similar velocity of 9.1 ± 0.6 μm s^{-1} in pure water under UV irradiation. Interestingly the PHI–SiO_2 microswimmer doesn't swam at a speed of 8.6 ± 0.7 μm s^{-1}, even though it doesn't contain any of the redox active material. Hence due to the large overpotential of the hydrogen evolution reactions (HER) on the PHI surface, self-diffusiophoresis by HER can be ruled out. These results clearly showed that these microswimmers can swim in pure water irrespective of the capping material without the addition of any extra fuel. However, in the presence of methanol and benzyl alcohol, the velocity of the micromotors doubled compared to that in pure water for all capping materials; the uncapped SiO_2 exhibited negligible variation in velocity in the presence of alcohol. The addition of 5 % MeOH to Pt–PHI increased the mean speed from 10.4 ± 0.6 μm s^{-1} to 20.4 ± 1.3 μm s^{-1} and that of Au–PHI increased from 9.1 ± 0.6 μm s^{-1} to 16.3 ± 1.4 μm s^{-1}. This is due to the efficient hole scavenging by the alcohols that prevent the recombination effect. The major mechanism in the propulsion of material is the self-diffusiophoresis resulting from the reaction of photogenerated electrons with oxygen. The major surface reactions were almost the same for all the materials. Notably, the charge carrier separation of the Janus motors capped with Au or Pt was found to increase. Therefore, oxygen reduction reactions are feasible in both the g-C_3N_4 and Au hemispheres. Additionally, the electron transfer from g-C_3N_4 to the metal caps resulted in an additional propulsion mechanism, i.e., self-electrophoresis. Furthermore, Sridhar et al. investigated the propulsion mechanism of the MNMs with the addition of fuel, H_2O_2 under visible light irradiation [77]. PHI–Pt, and PHI–Au microswimmers swim with a speed of 13.6 ± 1.1 and 24.6 ± 1.6 μm s^{-1}, respectively in 0.5 vol% H_2O_2 under visible light illumination (intensity of 1.6 W cm^{-2}). PHI–Pt microswimmers were also propelled at lower H_2O_2 concentrations of 0.05 % (13.2 ± 0.9 μm s^{-1}) and 0.5 % (13.6 ± 1.1 μm s^{-1}) but saturated after 1 % (16.5 ± 1.1 μm s^{-1}). On the other hand, the speed of the PHI–Au microswimmers increased with the increase of H_2O_2 concentration and decreased after an optimum concentration of 1 %. The propulsion can be explained based on the generation of reactive species such as ${}^{\bullet}OH$ and the decomposition of H_2O_2 by the active materials (Fig. 3).

The composite g-C_3N_4@carbon microsphere MNM in an H_2O_2 solution was propelled at a velocity of 167.97 $μms^{-1}$ under visible light irradiation with an intensity of 250 mW cm^{-2}. Here, the major propulsion mechanism was bubble-induced self-propulsion. An asymmetrical photocatalytic redox reaction occurs on the light incident region of the micromotor, which generates bubbles in this region. As a result, the micromotor is propelled in the direction of light (positive phototaxis). The photocatalytic oxidation reactions happen on the light side of the micromotor and O_2 is released from that side only for the motion of the micromotor. This motion is strengthened by the stacking effect of g-C_3N_4 on the CMS surface. Like other micromotors, the propulsion velocity heavily depends on the H_2O_2 concentration and light intensity; the O_2 bubble formation can also be varied by changing these parameters [80]. Cui et al. synthesized an isotropic g–C_3N_4–coated CMS composites with a Pt/Pd layer on one side of the material. This layer produced oxygen bubbles that propelled the micromotor at a velocity of 14.5 ± 3.4 μm s $^{-1}$ under visible light irradiation (880 mW cm $^{-2}$) with 7.5 % H_2O_2 as fuel [76]. Feng et al. studied the motion behavior of a similar composite micromotor with 3-D porous foam-like Fe_3O_4/f-C_3N_4. The diffusion coefficient of f-C_3N_4 in pure water was determined to be 0.27 $μm^2$ s^{-1}, which increased to 1.68 $μm^2$ s^{-1} with the addition of 0.2 % H_2O_2 solution under visible light irradiation. The diffusiophoretic propulsion by the Fenton reaction and photocatalytic reaction on f-C_3N_4 are the major responsible factors for the movement of the Fe_3O_4/f-C_3N_4 motor. These reactions generated more charged and noncharged components in the presence of higher concentrations of H_2O_2 and light intensity [75]. The 3D-printed/Fe_3O_4/C_3N_4 was propelled by the water-splitting reaction caused by the layer of the Al/Ga alloy. The speed of the micromotor depends on the dosage of the Al/Ga layer [83]. In this system, Al reacts with water to form H_2 gas and Aluminium hydroxide. The formation of H_2 gas is the driving force in the propulsion of the micromotor. However, the formation of Aluminum hydroxide hinders the further reaction, which is masked by the presence of the Ga layer.

The reaction on the catalytic surface has been determined as the key mechanism in most micromotors. Notably, the solution phase reaction can also result in the propulsion of the micromotor. For example, Rayaroth et al. reported on the propulsion of C_3N_4 and Janus Fe/g-C_3N_4 by the reaction of Cr(VI) with H_2O_2. The NTA calculated the diffusion

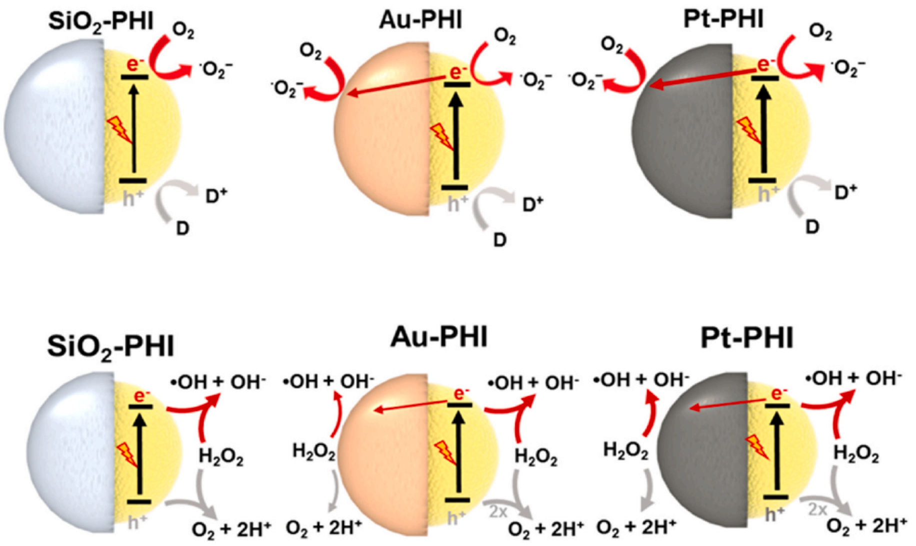

Fig. 3. Propulsion mechanism of metal-capped g-C_3N_4 without (in water) and with a fuel (H_2O_2). Reprinted with permission from Ref. [77].

coefficient (D) of the colloidal particles as a function of particle movement. The motion of particles was initiated by the Cr(VI)/H_2O_2 redox process under visible light irradiation. Notably, a significant improvement in the mobility of the particles was observed in the Cr(VI)/H_2O_2 system compared to that in pure water, Cr(VI), or H_2O_2 solutions [79]. Hence, a new mechanism was proposed in this case based on liquid phase O_2 generation rather than the surface of the micromotor (Fig. 4A). The proton-coupled electron transfer causes the reduction of Cr(VI) to Cr (III) with the formation of O_2 in the liquid phase (Eq. (6)) [91,92]. As given in Eq. (4), the photocatalytic reaction on g-C_3N_4 generated O_2 on their surface, and the bubbles were formed. The O_2 bubble generation by the liquid phase reaction (Eqn (6)) increased the nucleation process and thereby the size of the bubbles increased. This combined process increases the rate of diffusion of the particle.

$$HCr^{VI}O_4^- + 3H_2O_2 + 8H^+ \rightarrow 2Cr^{3+} + 3O_2 + 8H_2O \qquad (6)$$

In summary, the g–C_3N_4–based micromotor can be propelled via self-electrophoresis, self-diffusiophoresis, or bubble propulsion under visible light irradiation like other photocatalyst-based micromotors. g-C_3N_4 can photochemically oxidize H_2O_2 to generate O_2 bubbles, which are the driving force behind micromotor motion. Hence, it is proposed that metals (Pt, Pd, and Ag) can be replaced with g-C_3N_4 in micromotor design. However, modification of the micromotor should be done to improve their propulsion efficiency like their photocatalytic activity.

1.4. *Factors influencing the propulsion of g-C_3N_4 micromotors*

As posited in previous sections, the propulsion of the micromotor strongly depends on the intensity of the irradiated light and fuel concentration. Sridhar et al. found that both Pt and Au-g-C_3N_4 (poly(heptazine imides) (PHI)) were able to propel the micromotors with the same velocity in the presence of 2 % H_2O_2 as a fuel with a visible light intensity of 1.6 W cm^{-2}. Similarly, UV irradiation resulted in fast micromotor movement even with a low H_2O_2 concentration. The Pt and Au–PHI exhibited different properties with varying concentrations of H_2O_2. The velocity of the Pt–PHI becomes saturated at a fuel concentration of 0.5 %, while that of the Au–PHI increases with an increase in fuel concentration. Notably, the major mechanism here is self-diffusiophoresis. The presence of redox-active materials (Au or Pt) in one face of the MNM, leads to the decomposition of H_2O_2 and followed by the propulsion of the material. However, if the reaction happened on the redox-active face and g-C_3N_4 face the motion of the particle become

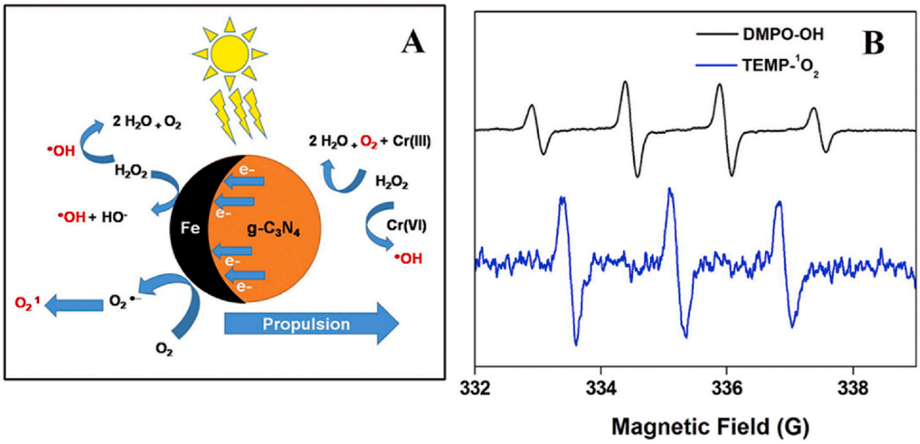

Fig. 4. Generation of ROS during the propulsion of Fe/g-C_3N_4 Janus micromotor in the Cr(VI) – H_2O_2 redox system. Reprinted with permission from Ref. [79] Copyright 2021 Elsevier.

slow down. The velocity of the tubular micromotor was found to increase with an increase in H_2O_2 concentration. The micromotors moved at a maximum velocity of 72 ± 6 μm s^{-1} at a fuel concentration of 30 % but moved at a velocity of 10 ± 6 μm s^{-1} at a fuel concentration of 10 %. Notably, the velocity of the composite tubular Fe_3O_4/g-C_3N_4 micromotor was observed to be higher, i.e., the velocity of the micromotor was determined to be 179 μm s^{-1} at an H_2O_2 concentration of 30 %. Similar behavior was observed in other micromotors, such as CMS and CS/g-C_3N_4, with varying H_2O_2 concentrations. In this case, the difference was that high-intensity visible light was used on CMS/g-C_3N_4 and a high concentration of H_2O_2 was provided. Additionally, Pt/Pd was coated on the CS/g-C_3N_4 surface for the decomposition of H_2O_2. The particles were able to be propelled at low H_2O_2 concentrations with low-intensity visible light. In the case of 3-D printed microbots, the speed of the micromotor depended on the dosage of the Al/Ga layer; the velocity of the particle increased with increasing in Al/Ga ratio, such that the frequency of water-splitting reactions was increased to generate more H_2 to propel the micromotor. As given in the previous sections the decomposition of H_2O_2 to O_2 bubbles by the active supporting materials on the micromotor is the major driving force. When the concentration of H_2O_2 is increased the O_2 bubble and subsequently the propulsion got increase.

In a Cr(VI)/H_2O_2 system, the velocity of the micromotor is dependent on the concentration of the Cr(VI), H_2O_2, and solution pH. Rayaroth et al. investigated the motion of the micromotor at varying Cr(VI), H_2O_2, and solution pH. Notably, the rate of diffusion of the micromotor in the presence of 5 ppm Cr(VI) was found to gradually increase from 8 nm^2 s^{-1} to 44 × 10^6 nm^2 s^{-1} with an increase in concentration from 0 % to 5 %. Similarly, the rate of diffusion of the micromotor in the presence of 5 % H_2O_2 increased from 12 nm^2 s^{-1} to 44 × 10^6 nm^2 s^{-1} with an increase in Cr(VI) concentration from 0 to 5 ppm. However, a further increase in the Cr(VI) concentration was found to reduce the rate of diffusion due to the formation of large bubbles in the liquid phase [79]. The study under varying pH shows that the rate of diffusion was maximum at a pH value of 6. The D value at pH 6 was 44 × 10^6 nm^2 s^{-1}. However, it was decreased to 28.7 × 10^6, and 27.5 × 10^6 nm^2 s^{-1} respectively with an increase in the values to 8, and 10. In addition, a lower D value of 24 × 10^6 nm^2 s^{-1} was observed at a lower pH of 2.5. The authors also tested the dissolution of Fe from Fe/g-C_3N_4 and showed that Fe concentration in the aqueous medium was 0.06, 0.013, and 0.015 mg L^{-1} at pHs 2.5, 8, and 10, respectively. On the other hand, the iron dissolution was very insignificant at pH 6. Thus, the Fe has a significant role as an electron acceptor in the generation of ROS and subsequently propulsion of micromotor.

In short, like other micromotor systems, the propulsion strongly depended on the light intensity in the case of photocatalytic micromotors, and fuel concentration (Eg: H_2O_2) in the case of fuel-driven micromotor. It is expected that with proper modification or by making structural defects, one can improve the efficiency of the micromotor with the minimum use of chemical fuels.

1.5. *The behavior of g-C_3N_4 micromotor under external stimuli*

As posited in previous sections, a majority of g-C_3N_4 micromotors are controlled by light and hence, the motion of these micromotors is affected by light intensity. Ye et al. studied the light-dependent movement of the Pt-g-C_3N_4 micromotor; the motion of the particles in the dark and under light, as well as the varying direction of the incident light, were reported. The particles were found to move in the direction of irradiated light and became immobile when the light was turned off. Ye et al. forced the micromotor into an "S" trajectory by varying the direction of the incident light (Fig. 5 I and II). The coating of amino-functionalized thiol on Pt-g-C_3N_4 could result in the formation of positively charged NH_2–Pt-g-C_3N_4. The positively charged micromotor also exhibited negative phototaxis properties. Additionally, Ye et al. studied the motion behavior of a group of micromotors. The motion of the

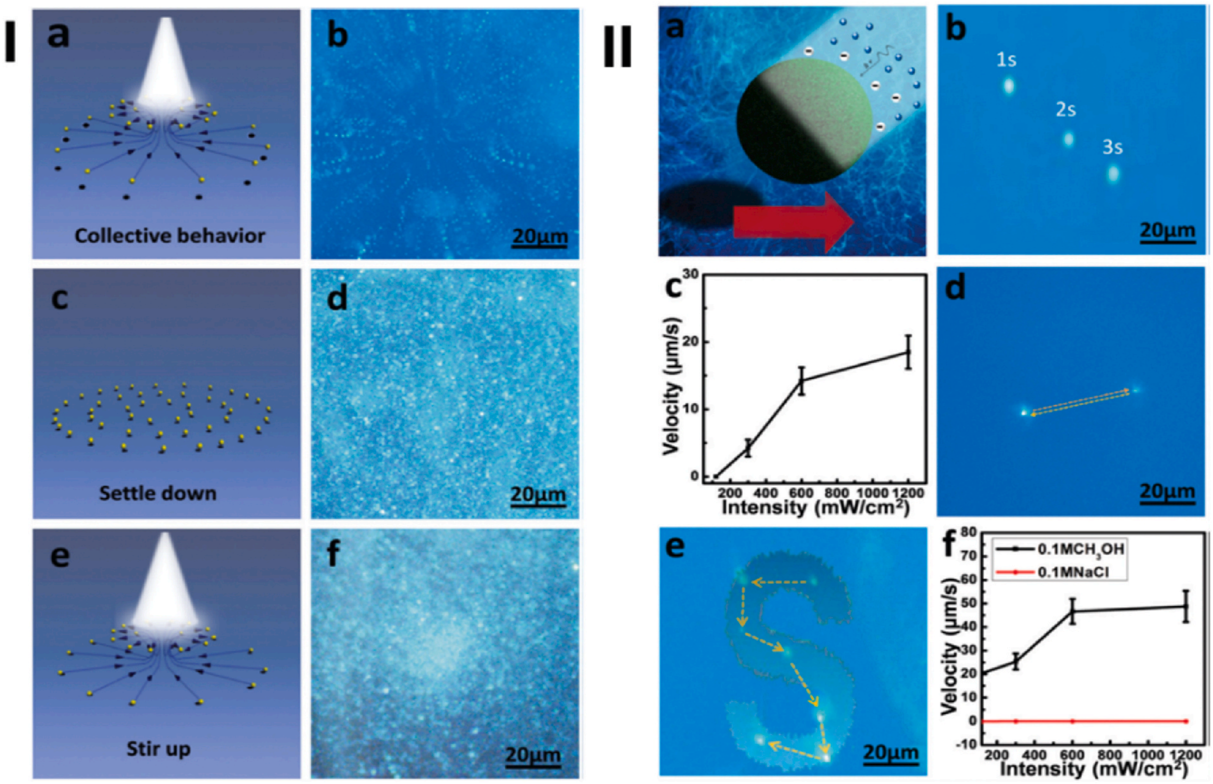

Fig. 5. Sedimentation and agitation of micromotors (I) Positive phototaxis behavior (II) of Pt-g-C_3N_4 micromotor under the influence of light irradiation. Reproduced with permission from Ref. [78] with permission from the Royal Society of Chemistry.

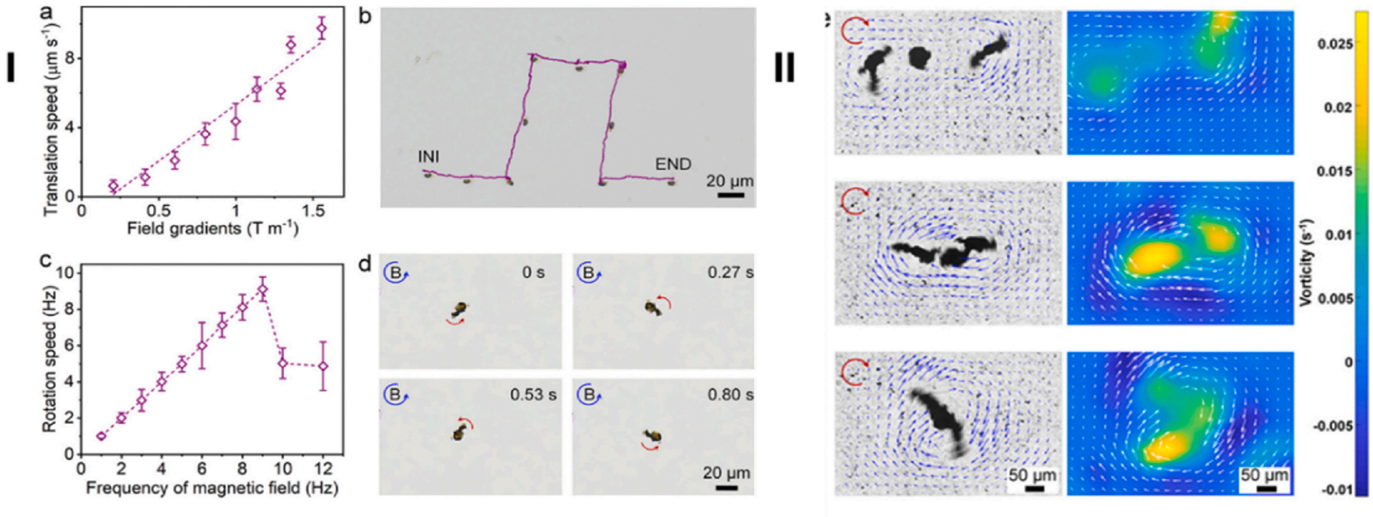

Fig. 6. The translational and rotational velocities of Fe_3O_4/f-C_3N_4 by varying their appropriate parameters (I). Aggregation of Fe_3O_4/f-C_3N_4 under a rotary magnetic field (II). Reproduced with permission from Ref. [75] Copyright 2022 American Chemical Society.

micromotors was found to be complex under light irradiation in the vertical direction. The particles in water initially moved toward the light because of their positive phototaxis properties and subsequently started to move away from the light. The motion behavior of the particles resulted in a change from a transparent solution to a turbid solution by light irradiation (Fig. 5 I) [78]. In this case, the bubble generation was completely inhibited when the light was turned off. The particle stopped moving when the light was turned off and resumed moving when the light was turned on. The dependence of the micromotors on the intensity of incident light was also noted (Fig. 5 II). When a Pt-g-C_3N_4 in water was irradiated with white light with an intensity of 600 mW cm^{-2}, it started to move towards the light at a velocity of 14 μm s^{-1}. The propulsion of the micromotor was directly proportional to the intensity of light and inversely proportional to the concentration or size of the particles. When the intensity was increased to 1200 mW cm^{-2}, the velocity increased to approximately 23 μm s^{-1}. The g-C_3N_4@CMS and tubular g-C_3N_4 micromotor also exhibited similar behavior under light irradiation [80,82].

The propulsion of the micromotor is also controlled by external magnetic fields, especially for materials with magnetic properties (Fig. 6). Feng et al. reported that the translational speed of Fe_3O_4/f-C_3N_4 increased in a magnetic field gradient. The micromotor moved at an increased velocity of 9.8 ± 0.6 μm s^{-1} in a magnetic field gradient of 1.6 T m^{-1}. The micromotor also exhibited a rotating motion under a rotary magnetic field due to the presence of the magnetic layer of Fe_3O_4; this motion is increased with an increase in the intensity of the rotary magnetic field. The rotation of the micromotor increased the local concentration of the catalyst via the convergence of the individual micromotor (Fig. 6) [75]. Zheng et al. also studied the performance of a tubular g-C_3N_4/Fe_3O_4 micromotor under a magnetic field. The tubular micromotor was propelled freely in an H_2O_2 solution without any magnetic field. However, when a magnetic field was applied, the micromotor was found to move toward the magnetic field [81].

The effect of heavy metals on the propulsion of tubular g-C_3N_4 micromotors was also analyzed. The micromotor was able to move through the matrix even at lower concentrations of H_2O_2 (5 wt%). Notably, the addition of 15 ppm of heavy metals such as Cu, Cr, Ni, Co, Cd, and Pb, into 5 wt% of H_2O_2 increased the velocity of the micromotor to 100, 31, 22, 14, 9, and 5 μm s^{-1}, respectively. This is due to the complexation reaction between the C and N-based functional groups from g-C_3N_4 and the above metal ions. This reaction facilitates the removal of these contaminants. In addition, the adsorbed metal ions could decompose H_2O_2 to generate more bubbles in the cavity and increase the velocity of the micromotors [82].

1.6. The application of g-C_3N_4 micromotor in the removal of pollutants

As a photocatalytic material, g-C_3N_4 produces many reactive oxygen species such as $^{\bullet}OH$, $O_2^{\bullet-}$, and $^1O_2$, which can oxidize organic contaminants (Eqs (7)–(10)) [39–41,87–89]. Additionally, the abundance of adsorption sites within these materials enhances the removal of heavy metals via complexation reactions and Lewis acid-base interactions [93–95]. Taking these advantages into account, the reviewed papers suggest that g-C_3N_4 micromotors can mainly be applied in water purification, especially in the removal of pollutants (Table 1).

$$H_2O + h^+ \rightarrow {}^{\bullet}OH + H^+, \tag{7}$$

$$H_2O_2 + e^- \rightarrow {}^{\bullet}OH + OH^-, \tag{8}$$

$$O_2 + e^- \rightarrow O_2^{\bullet-}, \tag{9}$$

$$O_2^{\bullet-} + H_2O \rightarrow {}^1O_2 + H_2O_2, \tag{10}$$

The propulsion of tubular g-C_3N_4 micromotors in the presence of H_2O_2 under visible light was found to be effective in the removal of Cu^{2+}. The autonomous motion of the material resulted in a 50 % removal of 15 ppm Cu^{2+} and 100 % removal of 1 ppm Cu^{2+} in 7 min, which is more effective than other adsorption experiments [82]. Metal complexation between N and C of the micromotor and Lewis acid-base interaction is the major mechanism in the adsorption of Cu^{2+} on the tubular micromotor. The isoelectric point of the tubular micromotor is 5 and hence it became negatively charged at the neutral pH condition, which favored a strong electrostatic interaction between the micromotor and Cu^{2+} ions.

The major reactive species detected in the Cr(VI)–H_2O_2 redox system were $^1O_2$ and $^{\bullet}OH$ (Fig. 4B), which is confirmed by the ESR [96]. These reactive species lead to the complete removal of sulfamethoxazole. The degradation efficiency was decreased with increasing concentration of SMX. A complete degradation was achieved with the lowest concentration of 1 ppm and only 50 % of the degradation was attained with the highest available concentration of 20 ppm. The role of ROS in degrading SMX was tested with various scavengers. In this case, the major species identified were $O_2^{\bullet-}$, and $^1O_2$ (degradation was decreased with *para*--benzoquinone and FFA). It is further evident from the scavenging test with hole scavengers (IPA and HCOOH) that might increase the $O_2^{\bullet-}$, and $^1O_2$. The degradation efficiency was increased with H_2O_2 and Cr (VI) concentration, as abundant reactive species can be expected with an increase of these reactants. In addition, the optimum pH for the effective degradation was found at 6. The degradation decreased all other lower and higher pH values. It showed that the Fe content of the micromotor played a prominent role in the degradation. The Fe content affected the electron storage capacity of the materials and subsequently the ROS generation. The dissolution of Fe was observed in all the pHs except that at 6, and hence can be clearly explained the degradation efficiencies under varying pHs. Additionally, Cr(VI) was reduced to Cr(III) by H_2O_2 in all the selected experimental conditions. Therefore, Fe/g-C_3N_4 micromotor can be utilized in the simultaneous removal of Cr(VI) and sulfamethoxazole. The mechanism of ROS generation in g-C_3N_4 in the Cr (VI)/H_2O_2 system is detailed in Fig. 4 [79].

The f-g-C_3N_4/Fe_3O_4 micromotor in contaminated water resulted in the rapid oxidation of tetracycline with the addition of 2 % H_2O_2 under visible light irradiation in a rotary magnetic field. Notably, only half of the pollutants were removed without the addition of H_2O_2. The propulsion of the micromotor increased the local concentration of the catalyst and hence increased the ROS formation. The Fe^{3+} to Fe^{2+} formation through the electron transfer reaction to Fe_3O_4, induces the Fenton oxidation. In this case, a photo-Fenton reaction was initiated with the addition of H_2O_2, resulting in the evolution of reactive oxygen species (ROS) such as $O_2^{\bullet -}$, $^{\bullet}OH$, and $^1O_2$ [75,97,98]. These species were identified from electron spin resonance (ESR). The tetracycline undergoes oxidation with these ROS to form several intermediate compounds, that further oxidize to lower chain molecules and finally to CO_2 and water.

Similar mechanisms were proposed for the tubular g-C_3N_4/Fe_3O_4, g-C_3N_4@CMS, and g-C_3N_4@CS micromotors for the oxidative degradation of organic dye molecules [76,80]. Tubular g-C_3N_4/Fe_3O_4 in the presence of H_2O_2 produced ROS and completely degraded the RhB in 30 min. The motion especially the self-rotation of the micromotor increases the micromixing and hence enables the interaction between the micromotor and pollutant for their removal (complete decolorisation). The authors also tested for other dye molecules such as methylene blue and Congo red, complete removal, but with different rates was achieved for both molecules. The environmental applicability of 3D-printed/Fe_3O_4/C_3N_4 was investigated by evaluating the oxidative degradation performance of the micromotor of an explosive, picric acid. The use of this micromotor resulted in a 38 % degradation of picric acid in 10 min [83]. The micromotors, especially the composites with Fe_3O_4, were able to be separated by an external magnetic field and reused for 5 cycles or more without any loss in propulsion and catalytic activity [75,81].

The g-C_3N_4 -based micromotors generated reactive species such as $^{\bullet}OH$, $O_2^{\bullet -}$, and $^1O_2$ that are very effective in the oxidative degradation of pollutants. The heavy metals can easily be adsorbed on the surface of the micromotor for their removal. In all the reported studies, a lower reaction volume was used and hence the scaling up of the process became thoroughly studied. The reaction volume should be increased to get a practical system and the experimental conditions should be investigated with those systems.

1.7. Summary, challenges, and future perspectives

Polymeric graphitic carbon nitride (g-C_3N_4) is a metal-free visible-light-active catalyst that has attracted attention for various environmental applications. Many micromotors have been developed using photocatalytic active materials, especially TiO_2. However, few reports have taken the advantages (metal-free, visible-light-active, and facile synthesis) of g-C_3N_4 into account in the fabrication of MNMs. g-C_3N_4 micromotors were propelled in aqueous media at very low fuel concentrations of H_2O_2 (or even without H_2O_2) under visible light irradiation. Compared to other photocatalytic micromotors, most of the micromotors reviewed in this paper are propelled by a bubble propulsion mechanism. The magnetic behavior of these materials makes them ideal for separation and reuse. Even though both spherical and tubular micromotors performed well in aqueous media and were able to effectively remove organic contaminants from the media, the tubular micromotors were effective in the removal of heavy metals.

Since the trajectories of MNMs are highly sensitive to their morphology, some specific shape is desired for their propulsion in the liquid environment. Therefore the fabrication step is challenging for those MNMs. Like other micromotors, bulk synthesis protocols for these micromotors need to be developed to study their practicability.

Unlike other photocatalytic micromotors, g-C_3N_4 micromotors have only been started recently. However, many factors limit the application of g-C_3N_4 as micromotors. Notably, charge separation affects the ability of the micromotors to be propelled under visible light irradiation. In future work, a Z-scheme catalyst based on g-C_3N_4 and other photocatalytic materials can be developed to promote charge separation and improve the light-harvesting power of the g-C_3N_4. The advantage of this material is that the *in situ* production of H_2O_2 mitigates the need for the external addition of fuel. The ability of g-C_3N_4 to decompose H_2O_2 to O_2 means that it can be utilized as a supporting material in the fabrication of micromotors. Hence the other toxic materials as supporting materials can be avoided.

Many factors are yet to be considered, such as the reusability of the micromotors as well as the adsorption efficiency of these micromotors in real contaminated water with co-existing ions. In addition, the knowledge on the propulsion of MNMs in the presence of co-existing matrices (ions, and organic matrices) is very scarce. Therefore a detailed study should be carried out to expand their use in environmental remediation. The removal efficiency should not be concluded with a single contaminant. Heavy metals with different charges and organic with different physicochemical properties should be tested to get a clear idea about their practical application.

The ecotoxicological effect of these micromotors is still not available and should be investigated as a part of the large-scale implementation. Therefore, the collective contribution of various researchers and scientists in various fields is crucial for the application of g-C_3N_4 in various industries.

CRediT authorship contribution statement

Manoj P. Rayaroth: Writing – review & editing, Writing – original draft, Methodology, Data curation, Conceptualization. **Giehyeon Lee:** Writing – review & editing, Funding acquisition. **Yoon-Seok Chang:** Writing – review & editing, Supervision, Resources, Funding acquisition.

Declaration of competing interest

The authors declare that they have no known competing financial interests or personal relationships that could have appeared to influence the work reported in this paper.

Data availability

Data will be made available on request.

Acknowledgment

This work was supported by the National Research Foundation of Korea (NRF) grant funded by the Korean government (MSIT). (2023R1A2C1006030). MPR is also thankful to GITAM (Deemed to Be) University, Visakhapatnam for providing all other facilities.

References

[1] M. Pelaez, N.T. Nolan, S.C. Pillai, M.K. Seery, P. Falaras, A.G. Kontos, P.S. M. Dunlop, J.W.J. Hamilton, J.A. Byrne, K. O'Shea, M.H. Entezari, D.D. Dionysiou, A review on the visible light active titanium dioxide photocatalysts for environmental applications, Appl. Catal. B Environ. 125 (2012) 331–349, https://doi.org/10.1016/j.apcatb.2012.05.036.

[2] J. Schneider, M. Matsuoka, M. Takeuchi, J. Zhang, Y. Horiuchi, M. Anpo, D. W. Bahnemann, Understanding TiO2 photocatalysis: mechanisms and materials, Chem. Rev. 114 (19) (2014) 9919–9986, https://doi.org/10.1021/cr5001892.

[3] J. Luo, S. Zhang, M. Sun, L. Yang, S. Luo, J.C. Crittenden, A critical review on energy conversion and environmental remediation of photocatalysts with remodeling crystal lattice, surface, and interface, ACS Nano 13 (9) (2019) 9811–9840, https://doi.org/10.1021/acsnano.9b03649.

[4] A. Nagar, T. Pradeep, Clean water through nanotechnology: needs, gaps, and fulfillment, ACS Nano 14 (6) (2020) 6420–6435, https://doi.org/10.1021/acsnano.9b01730.

[5] L. Soler, S. Sánchez, Catalytic nanomotors for environmental monitoring and water remediation, Nanoscale 6 (13) (2014) 7175–7182, https://doi.org/10.1039/C4NR01321B.

[6] M. Safdar, J. Simmchen, J. Jänis, Light-driven micro- and nanomotors for environmental remediation, Environ. Sci.: Nano 4 (8) (2017) 1602–1616, https://doi.org/10.1039/C7EN00367F.

[7] H. Eskandarloo, A. Kierulf, A. Abbaspourrad, Nano- and micromotors for cleaning polluted waters: focused review on pollutant removal mechanisms, Nanoscale 9 (37) (2017) 13850–13863, https://doi.org/10.1039/C7NR05494G.

[8] Z. Xiao, M. Wei, W. Wang, A review of micromotors in confinements: pores, channels, grooves, steps, interfaces, chains, and swimming in the bulk, ACS Appl. Mater. Interfaces 11 (7) (2019) 6667–6684, https://doi.org/10.1021/acsami.8b13103.

[9] S.K. Srivastava, M. Guix, O.G. Schmidt, Wastewater mediated activation of micromotors for efficient water cleaning, Nano Lett. 16 (1) (2016) 817–821, https://doi.org/10.1021/acs.nanolett.5b05032.

[10] X. Chen, C. Zhou, Y. Peng, Q. Wang, W. Wang, Temporal light modulation of photochemically active, oscillating micromotors: dark pulses, mode switching, and controlled clustering, ACS Appl. Mater. Interfaces 12 (10) (2020) 11843–11851, https://doi.org/10.1021/acsami.9b22342.

[11] H. Zhou, C.C. Mayorga-Martinez, S. Pané, L. Zhang, M. Pumera, Magnetically driven micro and nanorobots, Chem. Rev. 121 (8) (2021) 4999–5041, https://doi.org/10.1021/acs.chemrev.0c01234.

[12] W. Gao, M. D'Agostino, V. Garcia-Gradilla, J. Orozco, J. Wang, Multi-fuel driven Janus micromotors, Small 9 (3) (2013) 467–471, https://doi.org/10.1002/smll.201201864.

[13] T. Xu, F. Soto, W. Gao, V. Garcia-Gradilla, J. Li, X. Zhang, J. Wang, Ultrasound-modulated bubble propulsion of chemically powered microengines, J. Am. Chem. Soc. 136 (24) (2014) 8552–8555, https://doi.org/10.1021/ja504150e.

[14] W. Gao, A. Pei, J. Wang, Water-driven micromotors, ACS Nano 6 (9) (2012) 8432–8438, https://doi.org/10.1021/nn303309z.

[15] A. Eichler-Volf, T. Huang, F. Vazquez Luna, Y. Alsaadawi, S. Stierle, G. Cuniberti, M. Steinhart, L. Baraban, A. Erbe, Comparative studies of light-responsive swimmers: Janus nanorods versus spherical particles, Langmuir 36 (42) (2020) 12504–12512, https://doi.org/10.1021/acs.langmuir.0c01913.

[16] R. Dong, Y. Cai, Y. Yang, W. Gao, B. Ren, Photocatalytic micro/nanomotors: from construction to applications, Accounts Chem. Res. 51 (9) (2018) 1940–1947, https://doi.org/10.1021/acs.accounts.8b00249.

[17] R. Dong, Y. Hu, Y. Wu, W. Gao, B. Ren, Q. Wang, Y. Cai, Visible-light-driven BiOI-based Janus micromotor in pure water, J. Am. Chem. Soc. 139 (5) (2017) 1722–1725, https://doi.org/10.1021/jacs.6b09863.

[18] J. Zhang, F. Mou, Z. Wu, S. Tang, H. Xie, M. You, X. Liang, L. Xu, J. Guan, Simple-structured micromotors based on inherent asymmetry in crystalline phases: design, large-scale preparation, and environmental application, ACS Appl. Mater. Interfaces 11 (18) (2019) 16639–16646, https://doi.org/10.1021/acsami.9b03579.

[19] G. Zhao, M. Pumera, Geometric asymmetry driven Janus micromotors, Nanoscale 6 (19) (2014) 11177–11180, https://doi.org/10.1039/C4NR02393E.

[20] R. Dong, Q. Zhang, W. Gao, A. Pei, B. Ren, Highly efficient light-driven TiO2–Au Janus micromotors, ACS Nano 10 (1) (2016) 839–844, https://doi.org/10.1021/acsnano.5b05940.

[21] J. Frueh, S. Rutkowski, T. Si, M. Gai, C. Gao, S.I. Tverdokhlebov, G. Qiu, J. Schmitt, Q. He, Y.-X. Ren, J. Wang, Propulsion mechanisms of light-driven plasmonic colloidal micromotors, Advanced Photonics Research 3 (1) (2022) 2100189, https://doi.org/10.1002/adpr.202100189.

[22] Y. Li, F. Mou, C. Chen, M. You, Y. Yin, L. Xu, J. Guan, Light-controlled bubble propulsion of amorphous TiO2/Au Janus micromotors, RSC Adv. 6 (13) (2016) 10697–10703, https://doi.org/10.1039/C5RA26798F.

[23] S.K. Panda, N.A. Kherani, S. Debata, D.P. Singh, Bubble-propelled micro/nanomotors: a robust platform for the detection of environmental pollutants and biosensing, Materials Advances 4 (6) (2023) 1460–1480, https://doi.org/10.1039/D2MA00798C.

[24] C. Chen, E. Karshalev, J. Guan, J. Wang, Magnesium-based micromotors: water-powered propulsion, multifunctionality, and biomedical and environmental applications, Small 14 (23) (2018) 1704252, https://doi.org/10.1002/smll.201704252.

[25] C.-S. Lee, J. Gong, D.-S. Oh, J.-R. Jeon, Y.-S. Chang, Zerovalent-iron/Platinum Janus micromotors with spatially separated functionalities for efficient water decontamination, ACS Appl. Nano Mater. 1 (2) (2018) 768–776, https://doi.org/10.1021/acsanm.7b00223.

[26] M.P. Rayaroth, D. Oh, C.-S. Lee, Y.-S. Chang, Simultaneous removal of heavy metals and dyes in water using a MgO-coated Fe3O4 nanocomposite: role of micro-mixing effect induced by bubble generation, Chemosphere 294 (2022) 133788, https://doi.org/10.1016/j.chemosphere.2022.133788.

[27] Q.-l. Wang, C. Wang, R.-f. Dong, Q.-q. Pang, Y.-p. Cai, Steerable light-driven TiO2-Fe Janus micromotor, Inorg. Chem. Commun. 91 (2018) 1–4, https://doi.org/10.1016/j.inoche.2018.02.020.

[28] L. Wang, A. Kaeppler, D. Fischer, J. Simmchen, Photocatalytic TiO2 micromotors for removal of microplastics and suspended matter, ACS Appl. Mater. Interfaces 11 (36) (2019) 32937–32944, https://doi.org/10.1021/acsami.9b06128.

[29] L. Kong, C.C. Mayorga-Martinez, J. Guan, M. Pumera, Fuel-free light-powered TiO2/Pt Janus micromotors for enhanced nitroaromatic explosives degradation, ACS Appl. Mater. Interfaces 10 (26) (2018) 22427–22434, https://doi.org/10.1021/acsami.8b05776.

[30] M. Ussia, M. Urso, K. Dolezelikova, H. Michalkova, V. Adam, M. Pumera, Active light-powered antibiofilm ZnO micromotors with chemically programmable properties, Adv. Funct. Mater. 31 (27) (2021) 2101178, https://doi.org/10.1002/adfm.202101178.

[31] R. Dong, C. Wang, Q. Wang, A. Pei, X. She, Y. Zhang, Y. Cai, ZnO-based microrockets with light-enhanced propulsion, Nanoscale 9 (39) (2017) 15027–15032, https://doi.org/10.1039/C7NR05168A.

[32] B. Jang, A. Hong, H.E. Kang, C. Alcantara, S. Charreyron, F. Mushtaq, E. Pellicer, R. Büchel, J. Sort, S.S. Lee, B.J. Nelson, S. Pané, Multiwavelength light-responsive Au/B-TiO2 Janus micromotors, ACS Nano 11 (6) (2017) 6146–6154, https://doi.org/10.1021/acsnano.7b02177.

[33] T. Maric, M.Z.M. Nasir, R.D. Webster, M. Pumera, Tailoring metal/TiO2 interface to influence motion of light-activated Janus micromotors, Adv. Funct. Mater. 30 (9) (2020) 1908614, https://doi.org/10.1002/adfm.201908614.

[34] W.Z. Teo, H. Wang, M. Pumera, Beyond platinum: silver-catalyst based bubble-propelled tubular micromotors, Chem. Commun. 52 (23) (2016) 4333–4336, https://doi.org/10.1039/C6CC00115G.

[35] H. Wang, G. Zhao, M. Pumera, Beyond platinum: bubble-propelled micromotors based on Ag and MnO2 catalysts, J. Am. Chem. Soc. 136 (7) (2014) 2719–2722, https://doi.org/10.1021/ja411705d.

[36] D. Zhou, Y.C. Li, P. Xu, L. Ren, G. Zhang, T.E. Mallouk, L. Li, Visible-light driven Si–Au micromotors in water and organic solvents, Nanoscale 9 (32) (2017) 11434–11438, https://doi.org/10.1039/C7NR04161F.

[37] D. Zhou, Y.C. Li, P. Xu, N.S. McCool, L. Li, W. Wang, T.E. Mallouk, Visible-light controlled catalytic Cu2O–Au micromotors, Nanoscale 9 (1) (2017) 75–78, https://doi.org/10.1039/C6NR08088J.

[38] K. Villa, X. Domènech, U.M. García-Pérez, J. Peral, Optimization of the experimental conditions of hydrogen production by the Pt–(CdS/ZnS) system under visible light illumination, RSC Adv. 6 (43) (2016) 36681–36688, https://doi.org/10.1039/C6RA03241A.

[39] J. Wen, J. Xie, X. Chen, X. Li, A review on g-C3N4-based photocatalysts, Appl. Surf. Sci. 391 (2017) 72–123, https://doi.org/10.1016/j.apsusc.2016.07.030.

[40] J. Zhu, P. Xiao, H. Li, S.A.C. Carabineiro, Graphitic carbon nitride: synthesis, properties, and applications in catalysis, ACS Appl. Mater. Interfaces 6 (19) (2014) 16449–16465, https://doi.org/10.1021/am502925j.

[41] H. Sun, G. Zhou, Y. Wang, A. Suvorova, S. Wang, A new metal-free carbon hybrid for enhanced photocatalysis, ACS Appl. Mater. Interfaces 6 (19) (2014) 16745–16754, https://doi.org/10.1021/am503820h.

[42] J. Wang, S. Wang, A critical review on graphitic carbon nitride (g-C3N4)-based materials: preparation, modification and environmental application, Coord. Chem. Rev. 453 (2022) 214338, https://doi.org/10.1016/j.ccr.2021.214338.

[43] S. Cao, J. Low, J. Yu, M. Jaroniec, Polymeric photocatalysts based on graphitic carbon nitride, Adv. Mater. 27 (13) (2015) 2150–2176, https://doi.org/10.1002/adma.201500033.

[44] F. Ding, D. Yang, Z. Tong, Y. Nan, Y. Wang, X. Zou, Z. Jiang, Graphitic carbon nitride-based nanocomposites as visible-light driven photocatalysts for environmental purification, Environ. Sci.: Nano 4 (7) (2017) 1455–1469, https://doi.org/10.1039/C7EN00255F.

[45] B.V. Lotsch, M. Döblinger, J. Sehnert, L. Seyfarth, J. Senker, O. Oeckler, W. Schnick, Unmasking melon by a complementary approach employing electron diffraction, solid-state NMR spectroscopy, and theoretical calculations—structural characterization of a carbon nitride polymer, Chem. Eur J. 13 (17) (2007) 4969–4980, https://doi.org/10.1002/chem.200601759.

[46] S. Bhowmik, S.J. Phukan, N.K. Sah, M. Roy, S. Garai, P.K. Iyer, Review of graphitic carbon nitride and its composite catalysts for selective reduction of CO2, ACS Appl. Nano Mater. 4 (12) (2021) 12845–12890, https://doi.org/10.1021/acsanm.1c02896.

[47] W.-J. Ong, L.-L. Tan, Y.H. Ng, S.-T. Yong, S.-P. Chai, Graphitic carbon nitride (g-C3N4)-based photocatalysts for artificial photosynthesis and environmental remediation: are we a step closer to achieving sustainability? Chem. Rev. 116 (12) (2016) 7159–7329, https://doi.org/10.1021/acs.chemrev.6b00075.

[48] P. Chincholikar, K.R.B. Singh, A. Natarajan, R.G. Kerry, J. Singh, J. Malviya, R. P. Singh, Green nanobiopolymers for ecological applications: a step towards a sustainable environment, RSC Adv. 13 (18) (2023) 12411–12429, https://doi.org/10.1039/D2RA07707H.

[49] J.C.G. Sousa, A.R. Ribeiro, M.O. Barbosa, M.F.R. Pereira, A.M.T. Silva, A review on environmental monitoring of water organic pollutants identified by EU guidelines, J. Hazard Mater. 344 (2018) 146–162, https://doi.org/10.1016/j.jhazmat.2017.09.058.

[50] A.L. Srivastav, M. Ranjan, Chapter 1 - Inorganic water pollutants, in: P. Devi, P. Singh, S.K. Kansal (Eds.), Inorganic Pollutants in Water, Elsevier2020, pp. 1-15. https://doi.org/https://doi.org/10.1016/B978-0-12-818965-8.00001-9.

[51] P. Verma, J.K. Ratan, Chapter 5 - Assessment of the negative effects of various inorganic water pollutants on the biosphere—an overview, in: P. Devi, P. Singh, S. K. Kansal (Eds.), Inorganic Pollutants in Water, Elsevier2020, pp. 73-96. https://doi.org/https://doi.org/10.1016/B978-0-12-818965-8.00005-6.

[52] S. Kurwadkar, Occurrence and distribution of organic and inorganic pollutants in groundwater, Water Environ. Res. 91 (10) (2019) 1001–1008, https://doi.org/10.1002/wer.1166.

[53] Y. Cao, X. Li, Adsorption of graphene for the removal of inorganic pollutants in water purification: a review, Adsorption 20 (5) (2014) 713–727, https://doi.org/10.1007/s10450-014-9615-y.

[54] A.A. Al-Raad, M.M. Hanafiah, Removal of inorganic pollutants using electrocoagulation technology: a review of emerging applications and mechanisms, J. Environ. Manag. 300 (2021) 113696, https://doi.org/10.1016/j.jenvman.2021.113696.

[55] G. Crini, E. Lichtfouse, Advantages and disadvantages of techniques used for wastewater treatment, Environ. Chem. Lett. 17 (1) (2019) 145–155, https://doi.org/10.1007/s10311-018-0785-9.

[56] I. Ali, New generation adsorbents for water treatment, Chem. Rev. 112 (10) (2012) 5073–5091, https://doi.org/10.1021/cr300133d.

[57] N. Puri, A. Gupta, A. Mishra, Recent advances on nano-adsorbents and nanomembranes for the remediation of water, J. Clean. Prod. 322 (2021) 129051, https://doi.org/10.1016/j.jclepro.2021.129051.

[58] S. Linley, N.R. Thomson, Environmental applications of nanotechnology: nano-enabled remediation processes in water, soil and air treatment, Water, Air, Soil Pollut. 232 (2) (2021) 59, https://doi.org/10.1007/s11270-021-04985-9.

[59] A.S. Adeleye, J.R. Conway, K. Garner, Y. Huang, Y. Su, A.A. Keller, Engineered nanomaterials for water treatment and remediation: costs, benefits, and applicability, Chem. Eng. J. 286 (2016) 640–662, https://doi.org/10.1016/j.cej.2015.10.105.

[60] M.E.A. El-sayed, Nanoadsorbents for water and wastewater remediation, Sci. Total Environ. 739 (2020) 139903, https://doi.org/10.1016/j.scitotenv.2020.139903.

[61] S. Zinatloo-Ajabshir, S. Rakhshani, Z. Mehrabadi, M. Farsadrooh, M. Feizi-Dehnayebi, S. Rakhshani, M. Dušek, V. Eigner, S. Rtimi, T.M. Aminabhavi, Novel rod-like [Cu(phen)2(OAc)]·PF6 complex for high-performance visible-light-driven photocatalytic degradation of hazardous organic dyes: DFT approach, Hirshfeld and fingerprint plot analysis, J. Environ. Manag. 350 (2024) 119545, https://doi.org/10.1016/j.jenvman.2023.119545.

[62] S. Zinatloo-Ajabshir, E. Shafaati, A. Bahrami, Facile fabrication of efficient Pr2Ce2O7 ceramic nanostructure for enhanced photocatalytic performances under solar light, Ceram. Int. 48 (17) (2022) 24695–24705, https://doi.org/10.1016/j.ceramint.2022.05.116.

[63] Z. Salehi, S. Zinatloo-Ajabshir, M. Salavati-Niasari, Novel synthesis of Dy2Ce2O7 nanostructures via a facile combustion route, RSC Adv. 6 (32) (2016) 26895–26901, https://doi.org/10.1039/C5RA27919D.

[64] M.P. Rayaroth, U.K. Aravind, C.T. Aravindakumar, Photocatalytic degradation of lignocaine in aqueous suspension of TiO2 nanoparticles: mechanism of degradation and mineralization, J. Environ. Chem. Eng. 6 (3) (2018) 3556–3564, https://doi.org/10.1016/j.jece.2017.10.050.

[65] P.V. Gayathri, M.P. Rayaroth, C.T. Aravindakumar, D. Pillai, S. Joseph, SUNLIGHT-INDUCED decontamination of water from emerging pharmaceutical pollutants using ZnO nanoparticles, Chemosphere 343 (2023) 140265, https://doi.org/10.1016/j.chemosphere.2023.140265.

[66] K. Xie, J. Fang, L. Li, J. Deng, F. Chen, Progress of graphite carbon nitride with different dimensions in the photocatalytic degradation of dyes: a review, J. Alloys Compd. 901 (2022) 163589, https://doi.org/10.1016/j.jallcom.2021.163589.

[67] C. Zhou, Z. Zeng, G. Zeng, D. Huang, R. Xiao, M. Cheng, C. Zhang, W. Xiong, C. Lai, Y. Yang, W. Wang, H. Yi, B. Li, Visible-light-driven photocatalytic degradation of sulfamethazine by surface engineering of carbon nitride : Properties, degradation pathway and mechanisms, J. Hazard Mater. 380 (2019) 120815, https://doi.org/10.1016/j.jhazmat.2019.120815.

[68] L. Jiang, X. Yuan, Y. Pan, J. Liang, G. Zeng, Z. Wu, H. Wang, Doping of graphitic carbon nitride for photocatalysis: a review, Appl. Catal. B Environ. 217 (2017) 388–406, https://doi.org/10.1016/j.apcatb.2017.06.003.

[69] B. Xu, M.B. Ahmed, J.L. Zhou, A. Altaee, G. Xu, M. Wu, Graphitic carbon nitride based nanocomposites for the photocatalysis of organic contaminants under visible irradiation: progress, limitations and future directions, Sci. Total Environ. 633 (2018) 546–559, https://doi.org/10.1016/j.scitotenv.2018.03.206.

[70] M. Ismael, A review on graphitic carbon nitride (g-C3N4) based nanocomposites: synthesis, categories, and their application in photocatalysis, J. Alloys Compd. 846 (2020) 156446, https://doi.org/10.1016/j.jallcom.2020.156446.

[71] F. Dong, L. Wu, Y. Sun, M. Fu, Z. Wu, S.C. Lee, Efficient synthesis of polymeric g-C3N4 layered materials as novel efficient visible light driven photocatalysts, J. Mater. Chem. 21 (39) (2011) 15171–15174, https://doi.org/10.1039/C1JM12844B.

[72] F. Dong, Y. Sun, L. Wu, M. Fu, Z. Wu, Facile transformation of low cost thiourea into nitrogen-rich graphitic carbon nitride nanocatalyst with high visible light photocatalytic performance, Catal. Sci. Technol. 2 (7) (2012) 1332–1335, https://doi.org/10.1039/C2CY20049J.

[73] S. Hwang, S. Lee, J.-S. Yu, Template-directed synthesis of highly ordered nanoporous graphitic carbon nitride through polymerization of cyanamide, Appl. Surf. Sci. 253 (13) (2007) 5656–5659, https://doi.org/10.1016/j.apsusc.2006.12.032.

[74] Q. Gu, Z. Gao, C. Xue, Self-sensitized carbon nitride microspheres for long-lasting visible-light-driven hydrogen generation, Small 12 (26) (2016) 3543–3549, https://doi.org/10.1002/smll.201600181.

[75] K. Feng, J. Gong, J. Qu, R. Niu, Dual-mode-driven micromotor based on foam-like carbon nitride and Fe3O4 with improved manipulation and photocatalytic performance, ACS Appl. Mater. Interfaces 14 (39) (2022) 44271–44281, https://doi.org/10.1021/acsami.2c10590.

[76] Y. Cui, X. Sheng, P.R. Anusuyadevi, M. Lawoko, A.J. Svagan, Self-assembled carbon spheres prepared from abundant lignin and urea for photocatalytic and self-propelling applications, Carbon Trends 3 (2021) 100040, https://doi.org/10.1016/j.cartre.2021.100040.

[77] V. Sridhar, F. Podjaski, J. Kröger, A. Jiménez-Solano, B.-W. Park, B.V. Lotsch, M. Sitti, Carbon nitride-based light-driven microswimmers with intrinsic photocharging ability, Proc. Natl. Acad. Sci. USA 117 (40) (2020) 24748–24756.

[78] Z. Ye, Y. Sun, H. Zhang, B. Song, B. Dong, A phototactic micromotor based on platinum nanoparticle decorated carbon nitride, Nanoscale 9 (46) (2017) 18516–18522, https://doi.org/10.1039/C7NR05896A.

[79] M.P. Rayaroth, D. Oh, C.-S. Lee, N. Kumari, I.S. Lee, Y.-S. Chang, Carbon-nitride-based micromotor driven by chromate-hydrogen peroxide redox system: application for removal of sulfamethaxazole, J. Colloid Interface Sci. 597 (2021) 94–103, https://doi.org/10.1016/j.jcis.2021.03.164.

[80] X. Song, Y. Tao, J. Liu, J. Lin, P. Dai, Q. Wang, W. Li, W. Chen, C. Zheng, Photocatalytic-induced bubble-propelled isotropic g-C3N4-coated carbon microsphere micromotors for dynamic removal of organic pollutants, RSC Adv. 12 (21) (2022) 13116–13126, https://doi.org/10.1039/D2RA01577C.

[81] C. Zheng, X. Song, Q. Gan, J. Lin, High-efficiency removal of organic pollutants by visible-light-driven tubular heterogeneous micromotors through a photocatalytic Fenton process, J. Colloid Interface Sci. 630 (2023) 121–133, https://doi.org/10.1016/j.jcis.2022.10.021.

[82] K. Villa, C.L. Manzanares Palenzuela, Z. Sofer, S. Matějková, M. Pumera, Metal-free visible-light photoactivated C3N4 bubble-propelled tubular micromotors with inherent fluorescence and on/off capabilities, ACS Nano 12 (12) (2018) 12482–12491, https://doi.org/10.1021/acsnano.8b06914.

[83] B. Khezri, K. Villa, F. Novotný, Z. Sofer, M. Pumera, Smartdust 3D-printed graphene-based Al/Ga robots for photocatalytic degradation of explosives, Small 16 (33) (2020) 2002111, https://doi.org/10.1002/smll.202002111.

[84] Y. Mei, A.A. Solovev, S. Sanchez, O.G. Schmidt, Rolled-up nanotech on polymers: from basic perception to self-propelled catalytic microengines, Chem. Soc. Rev. 40 (5) (2011) 2109–2119, https://doi.org/10.1039/C0CS00078G.

[85] A. McGlasson, L.C. Bradley, Investigating time-dependent active motion of Janus micromotors using dynamic light scattering, Small 17 (52) (2021) 2104926, https://doi.org/10.1002/smll.202104926.

[86] S. Lee, N. Kumari, K.-W. Jeon, A. Kumar, S. Kumar, J.H. Koo, J. Lee, Y.-K. Cho, I. S. Lee, Monofacet-selective cavitation within solid-state silica-nanoconfinement toward Janus iron oxide nanocube, J. Am. Chem. Soc. 140 (45) (2018) 15176–15180, https://doi.org/10.1021/jacs.8b09869.

[87] X. Wang, S. Blechert, M. Antonietti, Polymeric graphitic carbon nitride for heterogeneous photocatalysis, ACS Catal. 2 (8) (2012) 1596–1606, https://doi.org/10.1021/cs300240x.

[88] G. Liao, Y. Gong, L. Zhang, H. Gao, G.-J. Yang, B. Fang, Semiconductor polymeric graphitic carbon nitride photocatalysts: the "holy grail" for the photocatalytic hydrogen evolution reaction under visible light, Energy Environ. Sci. 12 (7) (2019) 2080–2147, https://doi.org/10.1039/C9EE00717B.

[89] J. Liu, H. Wang, M. Antonietti, Graphitic carbon nitride "reloaded": emerging applications beyond (photo)catalysis, Chem. Soc. Rev. 45 (8) (2016) 2308–2326, https://doi.org/10.1039/C5CS00767D.

[90] F. Mou, Y. Li, C. Chen, W. Li, Y. Yin, H. Ma, J. Guan, Single-component TiO2 tubular microengines with motion controlled by light-induced bubbles, Small 11 (21) (2015) 2564–2570, https://doi.org/10.1002/smll.201403372.

[91] M. Pettine, L. Campanella, F.J. Millero, Reduction of hexavalent chromium by H2O2 in acidic solutions, Environ. Sci. Technol. 36 (5) (2002) 901–907, https://doi.org/10.1021/es010086b.

[92] K. Kim, J. Kim, A.D. Bokare, W. Choi, H.-I. Yoon, J. Kim, Enhanced removal of hexavalent chromium in the presence of H2O2 in frozen aqueous solutions, Environ. Sci. Technol. 49 (18) (2015) 10937–10944, https://doi.org/10.1021/acs.est.5b02702.

[93] R. Hu, X. Wang, S. Dai, D. Shao, T. Hayat, A. Alsaedi, Application of graphitic carbon nitride for the removal of Pb(II) and aniline from aqueous solutions, Chem. Eng. J. 260 (2015) 469–477, https://doi.org/10.1016/j.cej.2014.09.013.

[94] G. Xiao, Y. Wang, S. Xu, P. Li, C. Yang, Y. Jin, Q. Sun, H. Su, Superior adsorption performance of graphitic carbon nitride nanosheets for both cationic and anionic heavy metals from wastewater, Chin. J. Chem. Eng. 27 (2) (2019) 305–313, https://doi.org/10.1016/j.cjche.2018.09.028.

[95] S. Guo, K. Wu, Y. Gao, L. Liu, X. Zhu, X. Li, F. Zhang, Efficient removal of Zn(II), Pb(II), and Cd(II) in waste water based on magnetic graphitic carbon nitride materials with enhanced adsorption capacity, J. Chem. Eng. Data 63 (10) (2018) 3902–3912, https://doi.org/10.1021/acs.jced.8b00526.

[96] A.D. Bokare, W. Choi, Chromate-induced activation of hydrogen peroxide for oxidative degradation of aqueous organic pollutants, Environ. Sci. Technol. 44 (19) (2010) 7232–7237, https://doi.org/10.1021/es903930h.

[97] M.P. Rayaroth, C.T. Aravindakumar, N.S. Shah, G. Boczkaj, Advanced oxidation processes (AOPs) based wastewater treatment - unexpected nitration side reactions - a serious environmental issue: a review, Chem. Eng. J. 430 (2022) 133002, https://doi.org/10.1016/j.cej.2021.133002.

[98] M.P. Rayaroth, M. Marchel, G. Boczkaj, Advanced oxidation processes for the removal of mono and polycyclic aromatic hydrocarbons – a review, Sci. Total Environ. 857 (2023) 159043, https://doi.org/10.1016/j.scitotenv.2022.159043.